COMPUTATIONAL FLUID DYNAMICS ANALYSIS OF VERY HIGH TEMPERATURE GAS-COOLED REACTOR CAVITY COOLING SYSTEM

THERMAL HYDRAULICS

KEYWORDS: *reactor cavity cooling system, natural convection, radiation*

ANGELO FRISANI,[a]* YASSIN A. HASSAN,[a] and VICTOR M. UGAZ[b]

[a]*Texas A&M University, Department of Nuclear Engineering*
129 Zachry Engineering Center, College Station, Texas
[b]*Texas A&M University, Department of Chemical Engineering*
224 Jack E. Brown Building, College Station, Texas

Received May 25, 2010
Accepted for Publication November 2, 2010

The design of passive heat removal systems is one of the main concerns for the modular very high temperature gas-cooled reactors (VHTR) vessel cavity. The reactor cavity cooling system (RCCS) is a key heat removal system during normal and off-normal conditions. The design and validation of the RCCS is necessary to demonstrate that VHTRs can survive to the postulated accidents. The computational fluid dynamics (CFD) STAR-CCM+/V3.06.006 code was used for three-dimensional system modeling and analysis of the RCCS.

A CFD model was developed to analyze heat exchange in the RCCS. The model incorporates a 180-deg section resembling the VHTR RCCS experimentally reproduced in a laboratory-scale test facility at Texas A&M University. All the key features of the experimental facility were taken into account during the numerical simulations.

The objective of the present work was to benchmark CFD tools against experimental data addressing the behavior of the RCCS following accident conditions. Two cooling fluids (i.e., water and air) were considered to test the capability of maintaining the RCCS concrete walls' temperature below design limits. Different temperature profiles at the reactor pressure vessel (RPV) wall obtained from the experimental facility were used as boundary conditions in the numerical analyses to simulate VHTR transient evolution during accident scenarios.

Mesh convergence was achieved with an intensive parametric study of the two different cooling configurations and selected boundary conditions.

To test the effect of turbulence modeling on the RCCS heat exchange, predictions using several different turbulence models and near-wall treatments were evaluated and compared. The comparison among the different turbulence models analyzed showed satisfactory agreement for the temperature distribution inside the RCCS cavity medium and at the standpipes walls. For such a complicated geometry and flow conditions, the tested turbulence models demonstrated that the realizable k-ε model with two-layer all y^+ wall treatment performs better than the other k-ε and k-ω turbulence models when compared to the experimental results and the Reynolds stress transport turbulence model results.

A scaling analysis was developed to address the distortions introduced by the CFD model in simulating the physical phenomena inside the RCCS system with respect to the full plant configuration. The scaling analysis demonstrated that both the experimental facility and the CFD model achieve a satisfactory resemblance of the main flow characteristics inside the RCCS cavity region, and convection and radiation heat exchange phenomena are properly scaled from the actual plant.

*E-mail: a.frisani@neo.tamu.edu

I. INTRODUCTION

In the 2002 Generation IV International Forum, the concept of very high temperature gas-cooled reactor (VHTR) was presented as one of the next-generation nuclear power plant (NGNP) designs. The VHTR candidates are the prismatic and pebble-bed configurations. Various design and analysis tools are needed to calculate the behavior of the NGNP under normal, off-normal, and accident conditions. Thus, software tools and adequate experiments for their validation or "benchmarking" should be provided.

For light water reactor analysis, one-dimensional techniques were usually adequate for calculating the plant thermal-hydraulic behavior since the fluid temperatures were considerably below the limits that challenge the integrity of structural materials (e.g., the reactor pressure vessel), even under arduous conditions. This is not the case for the VHTR. Bulk outlet temperature for the VHTR should be >750°C (Ref. 1). This is one of the operating requirements for generation-IV plants to be satisfied by VHTRs.

Among all the possible design-basis accidents identified for the VHTR, the loss of heat transport system and shutdown cooling system and the loss-of-coolant accident (LOCA) event in conjunction with water ingress from failed shutdown cooling system [hereafter referred as pressurized conduction cooldown (PCC) scenario and depressurized conduction cooldown (DCC) scenario, respectively] are considered the most likely to lead to maximum vessel wall and fuel temperatures. The phenomena identification and ranking table process carefully identifies the possible scenarios and the associated phenomena.[1,2]

The thermal-fluid behavior of VHTR can be analyzed with computational fluid dynamics (CFD) codes, system codes, and severe accident codes.[3–9] Of these software types, CFD can be used to analyze the fluid dynamics in any portion of NGNP. The strength of CFD codes is their capability to analyze the presence of localized hot spots and thermal gradients. The largest impediment of using CFD codes is their computational requirements and the size of the problem that requires analysis.

The objective of the present research was to develop a qualification framework for CFD codes in the nuclear system safety analysis. The CFD code selected was the CD-ADAPCO commercial code STAR-CCM+/V3.06.006 (Ref. 10). The outcome of the present work was to identify the weakness in the code models for representing thermal-hydraulic phenomena expected to occur in the VHTR during both normal operation and accident conditions. Once the models that need to be developed are identified, appropriate experiments can be devised to support the model development, so that scaled representations of the full-size system can be rationally designed for model validation.

II. DESCRIPTION OF THE VHTR REACTOR

The reference VHTR designs are an extension of the earlier designs of the General Atomics gas turbine-modular helium reactor (GT-MHR) and the pebble bed modular reactor (PBMR). The target VHTR differs from these designs, mainly in that the reactor outlet temperature may be higher, and the VHTR is to produce hydrogen in addition to electricity. Both designs are assumed to have confinements. The two reactor system designs mainly differ in the core configuration, which is the prismatic or pebble-bed form of the reactor fuel, respectively.

Both designs rely on passive cooling during any loss-of-power or loss-of-coolant scenarios. The ultimate heat sink is the environment, and all excess heat can be transported to the environment without natural circulation cooling inside the vessel via heat conduction and radiation to the vessel walls. From the vessel walls the heat is transported to the environment via a combination of radiation and natural circulation transport using some form of reactor cavity cooling system (RCCS). Air is present in the confinement such that if the reactor depressurizes because of a leak in a pipe, air will ultimately enter the vessel by diffusion.

II.A. Reactor Cavity Cooling System

There is a major difference in the RCCS design between the two reference reactor configurations. The GT-MHR design has an air-cooled RCCS, while the PBMR design has a water-cooled RCCS. For both RCCS configurations, heat is radiated from the exterior of the reactor vessel wall to a series of heat exchangers that are oriented vertically and arranged in a circle around the exterior of the reactor vessel. Water/air flowing within these heat exchangers (ducts or standpipes) transports the heat to the exterior of the containment. The cooling fluid is ducted in from outside the containment to these heat exchangers and then outside the confinement. The heat exchangers can be designed with a circular or rectangular cross section. The main objective of the standpipes is to insure a correct cooling of the cavity system and to provide a barrier that separates the coolant flowing through the heat exchangers from the atmosphere inside the reactor/silo confinement. The air-cooled RCCS system is designed to be totally passive under all operating conditions and has no blowers to power the airflow through the heat exchangers. For the water-cooled RCCS, forced circulation is assumed during normal operation. In case of accident, natural circulation in the cooling pipes is assumed to maintain the concrete walls below design limits.[11]

II.B. Selection of the Reference Accident Scenario

On the basis of the experience gained by gas-cooled reactor designers and experimentalists,[12,13] the PCC and

DCC accident scenarios are considered the most demanding and most likely to lead to maximum vessel wall and fuel temperatures.

The PCC scenario begins from a 100% power condition and is initiated by a loss of forced flow and simultaneous failure of shutdown cooling system to start. The forced flow is assumed to ramp to zero in conjunction with the blower coastdown characteristics. The reactor trips immediately. The core heat-up slows down by the natural circulation cooling developed inside the core and the increase of heat removal by conduction and radiation cooling to the RCCS. Eventually, the core cools down when the heat removal by conduction and radiation becomes larger than the core decay heat, and the system approaches a safe shutdown state. The temperatures of concern are the fuel temperature and that of the vessel structural components. Consequently, two phases can be addressed: (a) the coastdown and (b) the heat-up and passive cooling phases.

The DCC scenario begins from a 100% power condition and is initiated by a double-ended guillotine break of both the cold and hot ducts. After the break, the reactor system blows down quickly. The reactor trips immediately to decrease the core power down to decay heat level. Helium discharge into the reactor cavity stops when the pressures of the reactor system and cavity equalize. The fuel temperature continues to increase and experiences the first peak when the core decay heat is balanced by the conduction and radiation cooling to the RCCS. During this phase, air remaining in the reactor cavity continuously enters into the reactor vessel by molecular diffusion, causing extensive graphite oxidation and generating a large amount of heat, which results in a second peak in the core temperature. Graphite oxidation stops when the air in the reactor vessel is depleted, and then the fuel temperature starts to decrease. The core decay heat is continually removed by the bulk natural circulation cooling and by the conduction and radiation cooling to the RCCS. Eventually, the core cools down when the heat removal by conduction and radiation cooling becomes larger than the core decay heat and the core reaches a safe shutdown state. The temperatures of concern are the fuel temperature and that of the vessel structural components. Three phases can be identified for the DCC event: (a) the blowdown, (b) the molecular diffusion, and (c) the air mixture natural convection phase.

II.C. Identification of the Major Phenomena for the RCCS

Heat removal by the RCCS during PCC event is the main path for cooling the vessel. The radial temperature gradient developed across the core heats the vessel wall. The transfer of heat from the vessel wall to the air ducts is mainly by radiation heat transfer. Simulations with CFD codes indicate that this is >80% of the total heat transfer, with convection by air in the cavity making up the balance.[11] The view factors for the reactor vessel communicating with the ducts are especially complex because both the vessel and standpipes geometry is cylindrical. In the cooldown phase, the hot plumes in the vessel head raise the temperature of the vessel wall at the top such that the vessel temperature might be the limiting condition.

The energy conducted through the duct walls (i.e., standpipes) from the reactor cavity is convected to the water/air inside the duct and is also radiated by the inner surfaces of the duct to adjacent surfaces. A buoyant head is established inside the ducts as the water/air heated by the duct walls expands, rises, and draws coolant fluid at the duct inlet. The heat transfer and pressure loss phenomena inside the ducts depend on the velocity profile at the wall. If local buoyancy at the wall is introduced, then the heat transfer and pressure loss processes operate in the mixed rather than forced convection mode.

Considering the DCC event, the air in the reactor cavity before the onset of the upset will contain water vapor. Some of this water vapor will be present in the mixture of gases that enter the break site during the air ingress phase. In addition, during the air ingress and natural convection phase, graphite dust may be discharged into the reactor cavity. The dust may settle on the RCCS heat transfer surfaces in the cavity, changing their heat transfer characteristics. During the air ingress and natural convection phases, some of the air in the cavity that was not vented to the environment will move into the reactor vessel and oxidize graphite surfaces.

III. TEXAS A&M UNIVERSITY EXPERIMENTAL FACILITY

A simple small test facility was constructed at Texas A&M University to measure the temperature distributions in the RCCS cavity.[14–16] The vessel was made of copper and was electrically heated via electrodes. The flange for the connection of the top and bottom parts of the pressure vessel was taken into account. The external box (resembling the RCCS concrete walls) was made of glass, and five aluminum rising pipes (i.e., standpipes) were placed inside the cavity. A movable rack with thermocouples was used for temperature measurement inside the cavity. The rack plane can be moved radially from the reactor pressure vessel (RPV) wall to the gap between the central standpipe and the adjacent one in such a way to have temperature measurements along the cavity height at different distances from the RPV wall, and in the gap between the standpipes. The air in the region between the vessel and the standpipes is at ambient pressure. Figure 1 shows the RCCS model of the experimental facility. Table I addresses the experimental facility characteristic dimensions.

The five standpipes were realized with an internal tube representing the downcomer and an external tube representing the riser. The cooling fluid (air or water, depending on the RCCS configuration chosen) enters the inner tube (i.e., the downcomer) flowing downward. Close to the bottom of the cavity, two openings per standpipe

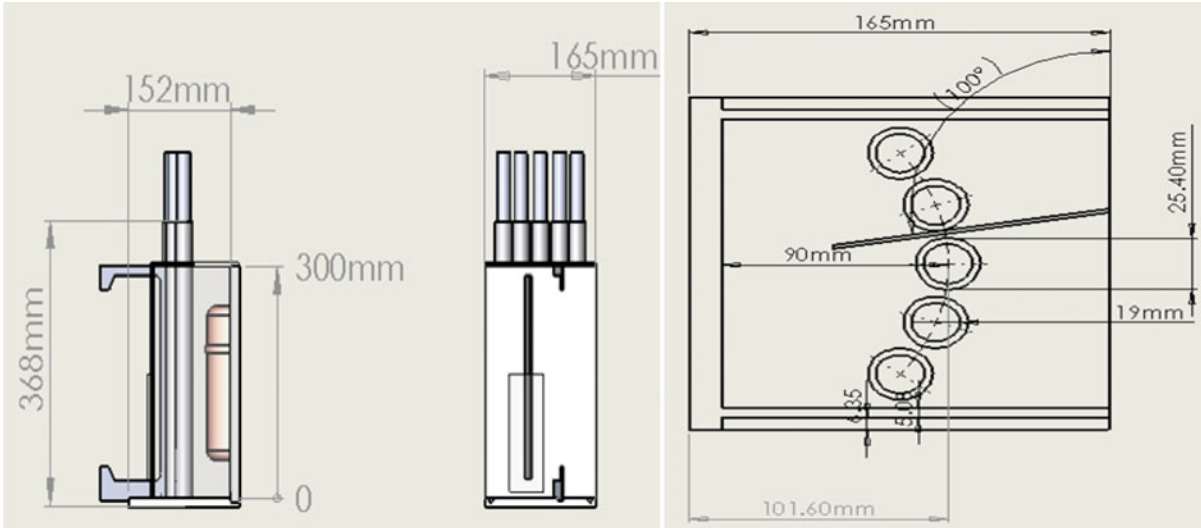

Fig. 1. Model of the Texas A&M University RCCS Experimental Facility (dimensions in mm).

TABLE I

Experimental Facility Dimensions

Dimensions	mm
Vessel height	200.0
Vessel radius	35.0
Gap vessel lower head—bottom wall	50.0
Gap vessel upper head—top wall	50.0
Total number of standpipes	5
Internal pipes height	445.0
Internal pipes diameter	19.0
Internal pipes thickness	0.75
External pipes height	368
External pipes diameter	25
Internal pipes thickness	0.7
Cavity height	300.0
Cavity length	127.0
Cavity width	125.0

on the inner tube surface allow the cooling fluid to be directed in the annulus between the inner and outer tubes. Because of buoyancy forces, the fluid moves upward in the riser cooling the standpipes in such a way to reduce the temperature at the RPV wall.

IV. TEXAS A&M UNIVERSITY EXPERIMENTAL FACILITY SCALING ANALYSIS

A scaling analysis of the RCCS Texas A&M University experimental facility was performed to demonstrate that the mock-up faithfully reproduces the main physical phenomena in the RCCS cavity for both the water-cooled and air-cooled configurations. Since no analytical information is available on the performance of a reference water-cooled and/or air-cooled RCCS, another objective of the scaling analysis was to determine a range of boundary conditions for the CFD analyses in such a way to have a preliminary description of the RCCS during accidents evolution. The STAR-CCM+/V.3.06.006 commercial CFD code[10] was challenged to perform these pretest analyses where many physical phenomena interact (integral test facility versus separate test facility approach). In fact, the analysis of the RCCS performance by CFD codes presents a number of challenging aspects as strong three-dimensional (3-D) effects in the RCCS cavity region and inside the standpipes, simulation of turbulence in flows characterized by natural circulation, high Rayleigh numbers and low Reynolds numbers, boundary layer separation and reattachment phenomena, radiation in very complex geometries, the potential of nucleate boiling in the tubes of the water-cooled configuration, very strong temperature gradients close to the vessel wall that require an accurate modeling for the change of air properties with temperature, etc.

The availability of experimental data allowed a preliminary estimate of the CFD performance benchmarking the numerical analyses for the temperature distribution inside the cavity with the experimental results obtained.

The analysis was carried out considering only the RCCS at steady-state conditions. The integral momentum equation in the axial direction for the standpipes can be written as follows:

$$p_{in} + \int_0^{L_h} (\rho g dL)_d = p_{out} + \int_0^{L_h} (\rho g dL)_u + \delta p_f + \delta \rho_l \ , \tag{1}$$

where

p_{in}, p_{out} = pressure at the standpipes inlet and outlet, respectively

ρ = coolant density

g = gravitational acceleration constant

L_h = heated length along the downcomer (subscript d) and the riser (subscript u).

As addressed in Sec. III, the downcomer and the riser of the Texas A&M University experimental facility have the same length with respect to the heated length; δp_f and δp_l represent the frictional and form pressure losses, respectively. The Boussinesq approximation can be used to link the density change with temperature for the fluid:

$$\rho(T) = \rho_0[1 - \beta(T - T_{in})] \ , \tag{2}$$

where

T = fluid temperature

β = volumetric coefficient of thermal expansion

ρ_0 = reference density (i.e., at the standpipes inlet)

T_{in} = temperature at the standpipes inlet.

A nondimensional temperature θ can be defined as function of the characteristic temperature difference across the standpipes $T_{out} - T_{in}$:

$$\theta = \frac{(T - T_{in})}{(T_{out} - T_{in})} \ . \tag{3}$$

Defining a characteristic velocity U_0 and a characteristic length L_r, the momentum equation [Eq. (1)] can be nondimensionalized as follows:

$$\frac{\Delta p}{\rho_0 U_0^2} - \frac{g\beta(T_{out} - T_{in})L_r}{U_0^2}\int_0^{l_h}(\theta dl)_d = -\frac{g\beta(T_{out} - T_{in})L_r}{U_0^2}\int_0^{l_h}(\theta dl)_u + \frac{1}{\rho_0 U_0^2}(\delta p_f + \delta p_l) \ , \tag{4}$$

where $l = L/L_r$. If the nondimensional Richardson number Ri is defined as

$$\mathrm{Ri} = \frac{g\beta(T_{out} - T_{in})L_r}{U_0^2} = \frac{g|\Delta\rho|L_r}{\rho_0 U_0^2} = \frac{\textit{buoyancy forces}}{\textit{inertia forces}} \ , \tag{5}$$

then Eq. (4) can be written as

$$\frac{\Delta p}{\rho_0 U_0^2} + \mathrm{Ri}\left[\int_0^{l_h}(\theta dl)_u - \int_0^{l_h}(\theta dl)_d\right] = \frac{1}{\rho_0 U_0^2}(\delta p_f + \delta p_l) \ . \tag{6}$$

The second term on the left side of Eq. (6) represents the contribution of buoyancy forces to the momentum equation, and the Ri number determines the relevance of buoyancy forces with respect to inertia forces in the standpipes.

Assuming a negligible effect of the standpipes downcomer in the energy balance equation (i.e., the coolant is mostly heated in the standpipes riser), it is possible to write a simplified energy balance equation in the standpipes annulus region:

$$A_{ann} U \rho c_p \frac{\partial T_e}{\partial Z} = P_e h_e (T_{se} - T_e) \ , \tag{7}$$

where

P_e, h_e = annulus external wall wetted perimeter and heat exchange coefficient, respectively

c_p = coolant fluid specific heat

A_{ann} = annulus cross-flow area

U = average coolant velocity in the standpipes annulus

T_e, T_{se} = coolant fluid temperature in the annulus region and the temperature at the annulus external wall, respectively.

Defining the nondimensional variable $z = Z/L_r$ and with $u = U/U_0$ and using the nondimensional temperature θ, Eq. (7) can be written in nondimensional form as

$$u\frac{\partial \theta_e}{\partial z} = \mathrm{St}_e(\theta_{se} - \theta_e) \ , \tag{8}$$

where St_e is the Stanton number at the annulus external wall and is defined as

$$\mathrm{St}_e = \frac{P_e h_e L_r}{\rho c_p U_0 A_{ann}} = \frac{\textit{heat transferred to the fluid}}{\textit{thermal capacity of the fluid}} \ . \tag{9}$$

As shown in Eq. (9), the St number represents a nondimensional ratio between the heat transferred to the fluid and the fluid thermal capacity.

Using the symmetry of the RCCS cavity, it is possible to assimilate its geometry to a rectangular two-dimensional cavity with one vertical wall heated, the other vertical wall cooled, and the two horizontal walls insulated. The conservation of mass, momentum, and energy equations can be written as

$$\frac{\partial W}{\partial Z} + \frac{\partial V}{\partial Y} = 0 \ , \tag{10}$$

$$\rho\left(W\frac{\partial W}{\partial Z} + V\frac{\partial W}{\partial Y}\right) = -\frac{\partial P}{\partial Z} - \rho_0 g[1-\beta(T-T_0)] + \mu\left(\frac{\partial^2 W}{\partial Z^2} + \frac{\partial^2 W}{\partial Y^2}\right) \ , \tag{11}$$

$$\rho\left(W\frac{\partial V}{\partial Z} + V\frac{\partial V}{\partial Y}\right) = -\frac{\partial P}{\partial Y} + \mu\left(\frac{\partial^2 V}{\partial Z^2} + \frac{\partial^2 V}{\partial Y^2}\right) \ , \tag{12}$$

and

$$\rho c_p\left(W\frac{\partial T}{\partial Z} + V\frac{\partial T}{\partial Y}\right) = k\left(\frac{\partial^2 T}{\partial Z^2} + \frac{\partial^2 T}{\partial Y^2}\right) \ , \tag{13}$$

where

P = pressure

W, V = velocity component in the vertical and horizontal directions, respectively

μ, k = air dynamic viscosity and thermal conductivity, respectively

ρ_0 = cavity air density at the reference temperature T_0.

The following nondimensional variables are defined as follows:

$$z = \frac{Z}{H} \ , \quad y = \frac{Y}{H} \ , \quad w = \frac{W}{u^*} \ , \quad v = \frac{V}{u^*} \ ,$$

$$p = \frac{P + \rho_0 g Z}{\rho u^{*2}} \ , \quad \theta = \frac{T - T_0}{T_h - T_c} \ , \tag{14}$$

where

T_h, T_c = average temperatures of the RPV wall and the standpipes external wall, respectively

H = RCCS cavity height, which is equal to the reference standpipes heated length L_r for the configuration chosen

u^* = reference air velocity in the cavity region (i.e., the maximum air velocity close to the RPV wall was considered).

Equations (10) through (13) can be written in nondimensional form as

$$\frac{\partial w}{\partial z} + \frac{\partial v}{\partial y} = 0 \ , \tag{15}$$

$$w\frac{\partial w}{\partial z} + v\frac{\partial w}{\partial y} = -\frac{\partial p}{\partial z} + \frac{\mathrm{Gr}}{\mathrm{Re}^2}\theta + \frac{1}{\mathrm{Re}}\left(\frac{\partial^2 w}{\partial z^2} + \frac{\partial^2 w}{\partial y^2}\right) \ , \tag{16}$$

$$w\frac{\partial v}{\partial z} + v\frac{\partial v}{\partial y} = -\frac{\partial p}{\partial y} + \frac{1}{\mathrm{Re}}\left(\frac{\partial^2 v}{\partial z^2} + \frac{\partial^2 v}{\partial y^2}\right) \ , \tag{17}$$

and

$$w\frac{\partial \theta}{\partial z} + v\frac{\partial \theta}{\partial y} = \frac{1}{\mathrm{Pe}}\left(\frac{\partial^2 \theta}{\partial z^2} + \frac{\partial^2 \theta}{\partial y^2}\right) \ . \tag{18}$$

Three new nondimensional numbers are defined: $\mathrm{Gr}/\mathrm{Re}^2$ is the Grashof number divided by the square of the Reynolds number, Re is the Reynolds number, and Pe is the Peclet number. The nondimensional $\mathrm{Gr}/\mathrm{Re}^2$ number is equal to

$$\frac{\mathrm{Gr}}{\mathrm{Re}^2} = \frac{\left(\dfrac{g\rho^2\beta(T_h - T_c)H^3}{\mu^2}\right)}{\left(\dfrac{\rho u^* H}{\mu}\right)^2} = \frac{g\beta(T_h - T_c)H}{u^{*2}}$$

$$= \frac{\textit{buoyancy forces}}{\textit{inertia forces}} \ . \tag{19}$$

The $\mathrm{Gr}/\mathrm{Re}^2$ number indicates the relevance of buoyancy forces respect to inertia forces, addressing the convection flow regime inside the RCCS cavity. For large $\mathrm{Gr}/\mathrm{Re}^2$ (i.e., $\mathrm{Gr}/\mathrm{Re}^2 \gg 1$), buoyancy forces prevail over inertial forces. This flow regime is called free convection. Vice versa, for small $\mathrm{Gr}/\mathrm{Re}^2$ (i.e., $\mathrm{Gr}/\mathrm{Re}^2 \ll 1$), inertia forces prevail over buoyancy forces. In these conditions the flow regime is forced convection. If $\mathrm{Gr}/\mathrm{Re}^2$ is of the order of unity, then mixed convection is present.

The nondimensional Re number represents the ratio between inertia and viscous forces:

$$\mathrm{Re} = \frac{\rho u^* H}{\mu} = \frac{\rho u^{*2}}{\mu\dfrac{u^*}{H}} = \frac{\textit{inertia forces}}{\textit{viscous forces}} \ . \tag{20}$$

The Pe number is defined as

$$\mathrm{Pe} = \mathrm{Re}\cdot\mathrm{Pr} = \frac{\rho u^* H}{\mu}\frac{\mu c_p}{k} = \frac{\rho c_p u^* \Delta T}{k\dfrac{\Delta T}{H}}$$

$$= \frac{\textit{heat transfer by advection}}{\textit{heat transfer by conduction}} \tag{21}$$

and represents a ratio between heat transfer by advection and heat transfer by conduction. Note that the definition of the Prandlt ($\mathrm{Pr} = \mu c_p/k$) number was used for the Pe number in Eq. (21).

If the Re number is assumed to be unity in the cavity region, then inertia forces are of the same order of magnitude of viscous forces. Under this assumption, the relation for the Gr number can be written as

$$\mathrm{Gr} = \frac{g\rho^2\beta(T_h - T_c)H^3}{\mu^2} = \frac{g|\Delta\rho|H}{\left(\frac{\mu^2}{\rho H^2}\right)} = \frac{g|\Delta\rho|H}{\left(\frac{\mu}{H}\cdot u^*\right)}$$

$$= \frac{\textit{buoyancy forces}}{\textit{viscous forces}} \quad . \tag{22}$$

Equation (22) represents the ratio of buoyancy forces over viscous forces, where buoyancy forces are the driving phenomenon and viscous forces are the dissipative phenomenon. For free convection flow regimes, the nondimensional Rayleigh number Ra can also be used to address the RCCS cavity convective flow regime:

$$\mathrm{Ra} = \mathrm{Gr}\cdot\mathrm{Pr} = \left(\frac{g\rho^2\beta(T_h - T_c)H^3}{\mu^2}\right)\cdot\left(\frac{\mu c_p}{k}\right)$$

$$= \frac{c_p g\rho^2\beta(T_h - T_c)H^3}{\mu k} \quad . \tag{23}$$

Considering an energy balance equation in the RCCS cavity between the RPV wall and the standpipes wall, the two main transfer mechanisms are radiation and convection. Therefore, a simplified energy balance equation in the cavity region can be written as

$$Q_0 = A_{conv}h_{cav}(T_h - T_c) + A_{rad}\varepsilon\sigma(T_h^4 - T_c^4) \quad , \tag{24}$$

where

Q_0 = energy from the RPV wall dissipated inside the standpipes

A_{conv}, A_{rad} = equivalent heat transfer area by convection and radiation, respectively

h_{cav} = reactor cavity heat transfer coefficient by convection

T_h = average temperature of the reactor vessel wall

T_c = average temperature of the external standpipes surface

σ = Stefan-Boltzmann constant

ε = surface emissivity.

The total energy dissipated inside the standpipes wall must equal the energy removed by the cooling fluid:

$$Q_0 = A_{ann}U_0\rho_0 c_p(T_{out} - T_{in}) \quad . \tag{25}$$

Using Eq. (25) it is possible to nondimensionalize Eq. (24), from which three additional similarity groups can be determined:

$$N_c = \frac{A_{conv}h_{cav}}{A_{ann}U_0\rho_0 c_p} \quad ,$$

$$N_r = \frac{A_{rad}\varepsilon\sigma T_{in}^4}{A_{ann}U_0\rho_0 c_p(T_{out} - T_{in})} \quad ,$$

and

$$N_t = \left(\frac{T_{out}}{T_{in}} - 1\right) \quad . \tag{26}$$

The cavity convective number N_c and radiation number N_r represent the fraction of energy transferred in the cavity region by convection and radiation heat exchange respect to the total energy transferred in the cavity, respectively.

Once similarity groups are determined for the physics of the problem under consideration, the objective of the scaling procedure is to determine the experimental facility geometrical dimensions and working conditions that would give similarity groups values very close to those obtained for the plant working conditions. This means that the goal of a scaling procedure is to obtain a unity ratio of as many similarity groups as possible between the experimental facility Π_m and the real plant Π_p:

$$\Pi_R = \frac{\Pi_m}{\Pi_p} \quad . \tag{27}$$

Table II shows the list of CFD simulations performed, with the boundary conditions imposed. Tests 1 through 4 refer to the water-cooled configuration, while tests 5 through 9 address the air-cooled RCCS configuration. For the water-cooled RCCS configuration, the heat source inside the RPV region was used as reference parameter. Table III shows the ratio of similarity groups for tests 1 through 4, where the high-temperature engineering test reactor was used as reference for the real plant geometry and working conditions.[11] The objective of these analyses was to simulate the real plant standpipes flow conditions and to study the behavior of the CFD model for convective and radiation numbers very close to those of the real plant configuration. A very small standpipes mass flow rate was set in such a way to simulate the same flow regime present in the real plant standpipes (i.e., natural circulation). The boundary conditions imposed for test 4 were congruent with the boundary conditions present in the experimental facility. This allowed a comparison of the nondimensional numbers,

TABLE II

CFD Simulations Imposed Boundary Conditions (Tests 1 Through 9)

Test Identification Number	RPV Power Generated (W)	U0 (m/s)
1 (water-cooled configuration)	27.0	0.0047
2 (water-cooled configuration)	50.0	0.0047
3 (water-cooled configuration)	175.0	0.0047
4 (water-cooled configuration)	196.0	0.410
5 (air-cooled configuration)	23.4	0.156
6 (air-cooled configuration)	43.16	0.156
7 (air-cooled configuration)	65.5	0.156
8 (air-cooled configuration)	104.2	0.156
9 (air-cooled configuration)	131.0	0.156

TABLE III

Ratio of Similarity Groups for Tests 1 Through 4 (Water-Cooled RCCS Configuration)

Ratio of Similarity Groups	Test 1	Test 2	Test 3	Test 4
Ri_R	0.112	0.208	0.728	1.22E−6[a]
St_R	12.76	12.76	12.76	5.22
$(Gr/Re^2)_R$	0.335	0.649	1.364	1.369
Ra_R	2.87E−7	5.55E−7	1.17E−6	1.17E−6
Nc_R	2.916	1.458	0.262	0.158
Nr_R	1.690	1.058	0.302	0.245
Nt_R	0.190	0.353	1.234	0.016

[a]Read as 1.22×10^{-6}.

addressing the main distortions introduced by the CFD model with respect to the mock-up and a benchmark of the CFD code with respect to the experimental data available.

With the low values of standpipes mass flow rate imposed as boundary condition for tests 1, 2, and 3, the CFD simulations introduce a limited distortion on the scaling of the buoyancy forces with respect to the inertia forces, which means that the ratio of Ri number between the experimental facility/CFD model and the real plant is close to unity, as addressed in Table III. The experiment for the water-cooled RCCS configuration (i.e., test 4) was performed under forced circulation standpipes conditions, and the contribution of buoyancy in the momentum equation can be neglected (i.e., the ratio of Ri number is much smaller than 1).

As addressed before, the St number measures the ratio of heat transferred to the fluid respect to the fluid thermal capacity. For the boundary conditions imposed in tests 1 through 4, the ratio of St number was >1, which means that the heat transferred in the experimental facility/CFD model is larger than the heat transferred in the real plane standpipes.

The ratio of Gr/Re^2 addresses the importance of buoyancy with respect to inertia forces in the RCCS cavity region. If the reference velocity for the CFD model and the real plant is assumed to be the maximum value of the air velocity close to the RPV wall—that is, where buoyancy forces are larger—the ratio of Gr/Re^2 number is very close to one for the boundary conditions imposed in tests 1 through 4, as shown in Table III. This means that the convective flow regime simulated in the CFD model is very close to that present in the real plant cavity region.

Using the definition of the Gr/Re^2 number given in Eq. (19), it is possible to determine the convective flow regime present in the experimental facility/CFD model cavity region. If the boundary conditions of test 4 are considered, the Gr/Re^2 number is

$$\left(\frac{\mathrm{Gr}}{\mathrm{Re}^2}\right)_m = \left(\frac{g\beta(T_h - T_c)H}{\mu^{*2}}\right)_m = \left(\frac{9.81 \cdot 0.0023 \cdot 250.0 \cdot 0.29}{0.35^2}\right) = 13.35 \quad . \tag{28}$$

With a Gr/Re^2 number >1, buoyancy forces are larger than inertia forces and free convection is present in the RCCS cavity region.

The Ra number for the experimental facility is six orders of magnitude smaller than the Ra number in the real plant. This difference is due to the different heated length for the mock-up and the real plant. The experimental facility/CFD model have a heated length two orders of magnitude smaller than the real plant heated length. As shown in Eq. (23), the ratio of Ra number is proportional to the third power of the heated length ratio [i.e., $(H_m/H_p)^3 = (1/100)^{-3} = 10^{-6}$]. Since the Ra number can be seen as a ratio between buoyancy forces and viscous forces, the conclusion is that the buoyancy forces that drive the flow inside the CFD model cavity are much smaller than those present in the real plant cavity region.

Figure 2 shows the ratio of convective N_c and radiation N_r numbers, which addresses the distortion introduced by the scaling on the heat transfer by convection and radiation in the RCCS cavity region, respectively. For the boundary conditions chosen for tests 1 through 4, both ratios are close to unity, which means that the scaled model does not introduce a relevant distortion with respect to the real plant in scaling convection and radiation heat transfer phenomena inside the cavity region.

CFD analyses were performed with air as cooling fluid in the RCCS standpipes (tests 5 through 9). The objective of the CFD analyses performed was to have a

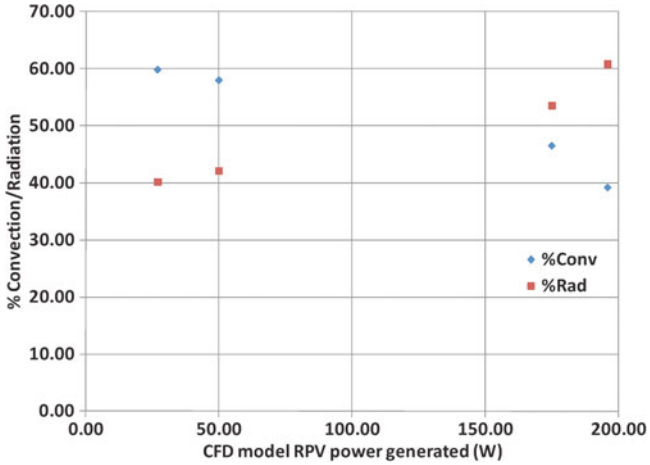

Fig. 2. Ratio of Nc and Nr numbers function of the RPV power generated (tests 1 through 4)

preliminary understanding of the RCCS system performances if air was used instead of water as cooling fluid in the standpipes. The numerical simulations performed for the RCCS with the air-cooled configuration covered a wide range of operating conditions. This allowed us to address the main differences between the two configurations and at the same time estimate whether the air-cooled configuration is suitable for maintaining the RCCS concrete wall temperature below design limits. A sensitivity analysis was performed on the power generated inside the RPV region, with the mass flow rate in the standpipes being constant (see Table II). The scaling analysis was carried out comparing the CFD model developed with the Natural Convection Shutdown Heat Removal Test Facility.[17] Table IV shows the ratio of similarity groups for tests 5 through 9.

From Table IV it is possible to conclude that for the air-cooled RCCS configuration, with the boundary conditions imposed for tests 5 through 9, the CFD model overestimates the effect of buoyancy in the standpipes with respect to the real plant standpipes (i.e., the ratio of Ri number is >1).

Also for the air-cooled configuration, the CFD model shows a larger heat exchange capacity for the standpipes with respect to the prototype (i.e., the ratio of St number is >1). The ratio of Gr/Re^2 is very close to unity, which means the CFD model does not introduce large distortions in simulating the physics inside the RCCS cavity region, correctly reproducing the convective flow regime.

Table IV shows that the CFD model introduces some distortions in simulating the heat exchange by radiation and convection inside the RCCS cavity region for the boundary conditions set in tests 5 through 9. On the other hand, Fig. 3 shows that the proportions between radiation and convection heat exchange in the cavity of the CFD model are in reasonable agreement with the values obtained from experimental data.[11] This means that the CFD model introduces the same amount of distortion for radiation and convection heat transfer mechanisms for the boundary conditions set in tests 5 through 9.

V. DESCRIPTION OF THE RCCS CFD MODEL DEVELOPED

The model developed to analyze heat exchange in the RCCS incorporates a 180-deg section resembling the VHTR RCCS test facility built at Texas A&M University.[14,15] All the key features of the experimental facility were taken into account. Figure 4 shows a detail of the central pipe. The fluid enters the system from the top through an internal duct in each of the five tubes and moves downward. Once the cooling fluid reaches the bottom of the standpipes, two openings per tube allow the fluid to enter an annulus, and the fluid moves upward, cooling the external pipe walls.

Two cooling fluids (water and air) were considered to test the capability of maintaining the RCCS concrete

TABLE IV

Ratio of Similarity Groups for Tests 5 Through 9

Ratio of Similarity Groups	Test 5	Test 6	Test 7	Test 8	Test 9
Ri_R	4.442	8.194	12.436	19.783	24.871
St_R	34.306	34.306	34.306	34.306	34.306
$(Gr/Re^2)_R$	0.356	0.452	0.729	0.910	1.044
Ra_R	1.59E−6[a]	2.02E−6	3.26E−6	4.07E−6	4.67E−6
Nc_R	16.805	8.403	5.042	1.846	0.975
Nr_R	29.186	15.216	10.026	6.302	5.013
Nt_R	0.669	1.246	1.891	3.008	3.782

[a]Read as 1.59×10^{-6}.

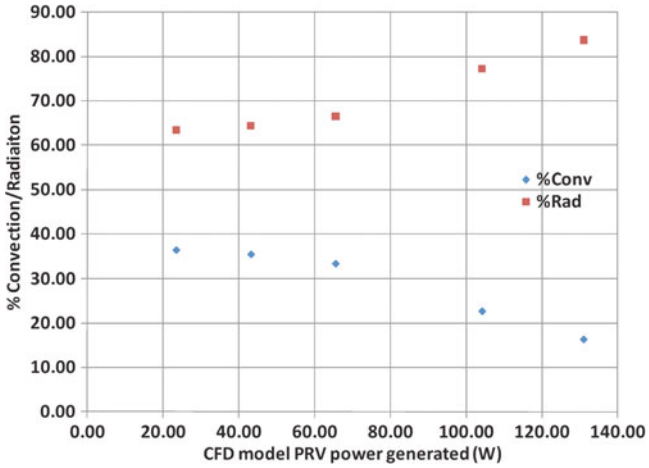

Fig. 3. Percentage of Nc and Nr numbers function of the RPV power generated (tests 5 through 9).

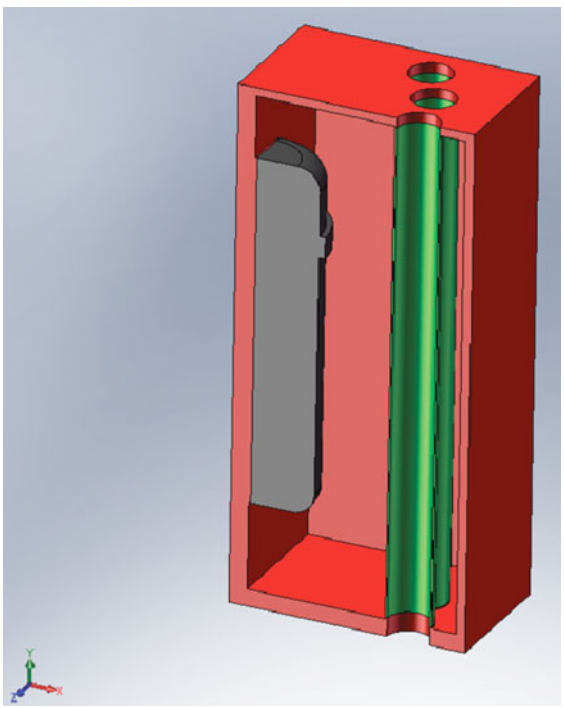

Fig. 4. CFD model of the Texas A&M University experimental facility.

wall temperature below design limits. Various boundary conditions were investigated to test the behavior of both water-cooled and air-cooled configurations under a wide range of RCCS working conditions, as discussed in Sec. IV.

In the analyses performed for the water-cooled RCCS configuration (tests 1, 2, and 3), the standpipes mass flow rate was kept constant, and the volumetric heat source boundary condition imposed inside the RPV region was used as reference parameter (see Table II). The sensitivity over the heat source boundary condition allowed us to address the behavior of the RCCS cavity scaled model for a wide range of scenarios from normal operation to transient conditions. For test 4, the RPV wall distribution for the CFD model was set equal to the one provided by the experimental data available. Also, the boundary conditions at the standpipes inlet were consistent with those used for the experimental analysis in test 4 (see Table II).

The CFD simulations of the RCCS air-cooled configurations were performed with a fixed temperature profile at the RPV wall and constant standpipes mass flow rate (tests 5 through 9). Because of the high thermal conductivity of the material used for the mock-up vessel (i.e., Cu), setting a constant heat source inside the RPV region is equivalent to an almost constant RPV wall temperature distribution. On the other hand, setting a temperature profile at the RPV wall allows us to address the nonuniform heat flux present on the vessel wall due to the location of the core region and the heat exchange inside the vessel. Table II gives the boundary conditions set for tests 5 through 9. The RPV power generated was obtained by integrating the total heat flux over the surface at the RPV wall.

A key point in the simulations of the RCCS cavity is the large temperature gradient present across the cavity region. Both experiments and CFD simulations were performed with the RPV wall at a very high temperature; meanwhile, the standpipe walls are at a relatively low temperature. For these conditions, it becomes very important to have an accurate estimate of the effect that buoyancy has on the airflow regime inside the RCCS cavity. Since the largest temperature gradients are close to the RPV wall, special care was taken in realizing the mesh close to the RPV wall. To reduce the errors due to mesh discretization, a very fine mesh was realized close to the RPV wall (Fig. 5). Five prism layers were generated at the RPV wall and at the interface between solid and fluid regions where conjugate heat transfer is present. The base size of the first prism layer was set equal to 0.1 mm, which translated to a maximum y^+ smaller than 0.1. This means that the viscous sublayer was correctly resolved.

Another important issue for a good representation of the buoyancy forces inside the RCCS cavity is linked to the change of air properties with temperature. This aspect was taken into account using Sutherland's law for air dynamic viscosity and thermal conductivity. For air inside the RCCS cavity, the ideal gas model was used (i.e., compressibility effects were taken into account).

To test grid independence, six different meshes were considered. Mesh convergence was reached with 11 202 000 cells. Table V gives the details of the meshes considered.

To take into account the heat losses present at the experimental facility external walls with the environment,

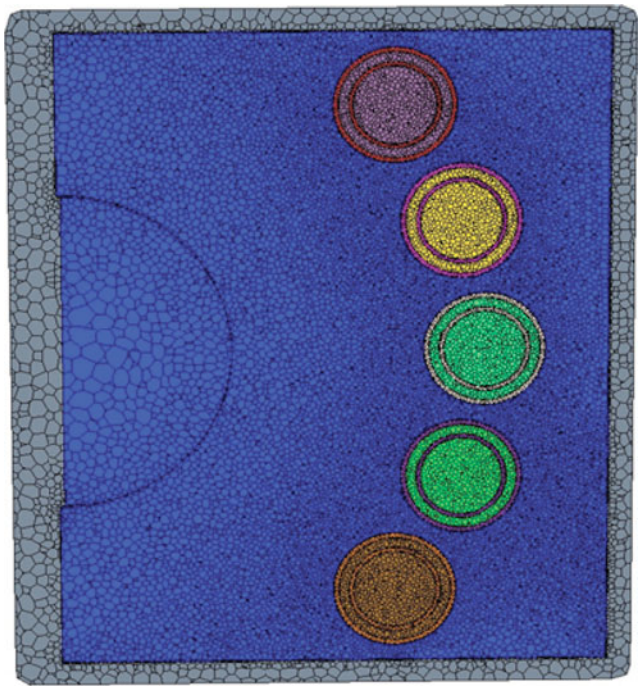

Fig. 5. CFD mesh of the Texas A&M University experimental facility (11 202 000 cells).

TABLE V

Mesh Sensitivity Analysis

Mesh Identification	Number of Total Cells	Number of Prism Layers
Fine1	2 360 842	2
Fine2	3 305 360	2
Fine3	5 191 149	2
Fine4	7 840 126	5
Fine5	10 775 153	5
Fine6	11 202 322	5

a convective heat boundary condition was set at the CFD model glass external wall. Sensitivity analyses were performed on the CFD model in such a way to have the same amount of energy dissipated by the experimental facility and the CFD simulations in the standpipes and at the external box walls. This allowed the CFD model to give a very close representation of the physics inside the experimental facility.

V.A. Description of the Turbulence Models Analyzed

To test the effect of turbulence modeling on the RCCS heat exchange, predictions using several different turbulence models and near-wall treatments were evaluated and compared. The models considered included the first-moment closure low–Reynolds number standard k-ε model[18] without wall function (*low* y^+) and a hybrid wall function (*all* y^+) treatment, the two-layer standard k-ε model[19,20] with a hybrid wall function (*all* y^+) treatment, the two-layer realizable k-ε model[21] with a hybrid wall function (*all* y^+) treatment, the low–Reynolds number Abe-Kondoh-Nagano (AKN) k-ε model[22] without wall function (*low* y^+) and a hybrid wall function (*all* y^+) treatment, the standard k-ω model[23] without wall function (*low* y^+) and a hybrid wall function (*all* y^+) treatment, the Menter Shear Stress Transport (SST) k-ω model[24] without wall function (*low* y^+) and a hybrid wall function (*all* y^+) treatment, the second-moment closure two-layer Reynolds stress transport (RST) model[25–27] with a hybrid wall function (*all* y^+) treatment, and the first-moment closure one-equation Spalart-Allmaras[28] without wall function (*low* y^+) and a hybrid wall function (*all* y^+) treatment. For the RST turbulence model applied, a linear pressure-strain model was used,[26] which splits the pressure-strain term in a slow (return-to-isotropy) term, a rapid term, and a wall-reflection term. A two-layer formulation for resolving the viscous sublayer was applied.

The segregated flow model for solving the momentum equations and the continuity equation for pressure was used for all simulations performed. For this solver the equations for the components of velocity and pressure are solved in an uncoupled manner. The linkage between the momentum and continuity equations is achieved with a predictor-corrector approach. The second-order upwind scheme was used for the convection term in all simulations performed.

VI. RESULTS AND DISCUSSION

The following discussion presents CFD simulation results for the RCCS water-cooled and air-cooled configurations. Comparisons with the different turbulence models used will be shown, and a discussion of the main physical phenomena present in the RCCS cavity and standpipes regions will be addressed.

VI.A. Analysis of the RCCS Water-Cooled Configuration (Tests 1 Through 4)

Figure 6 shows the sensitivity analysis over mesh refinement for the axial temperature distribution at the cavity region rack plane 5.0 mm from the RPV wall for test 1. Mesh convergence was tested progressively increasing the number of cells in the RCCS cavity and the standpipes regions. Because of the inherent instability of free convection and natural circulation phenomena, the residuals show some oscillatory behavior with a period of oscillation depending on mesh refinement and boundary conditions set. To analyze mesh convergence, an

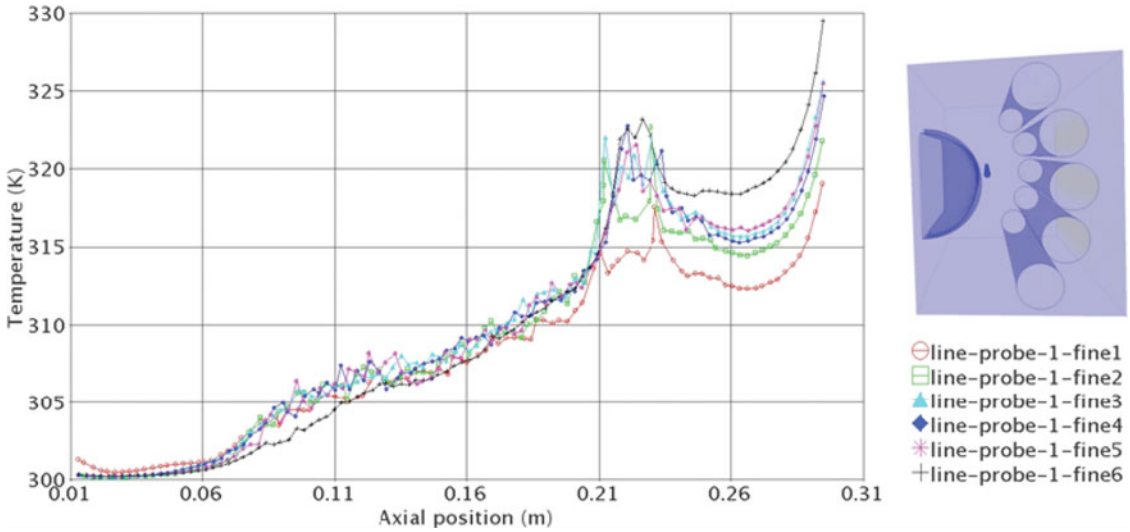

Fig. 6. Mesh sensitivity for the cavity region axial temperature distribution 5.0 mm from the RPV wall (rack plane)—test 1.

extensive analysis of temperature and velocity distributions was carried out in the RCCS cavity region. This criterion was used to judge mesh convergence for the analyses performed. The figure shows that there are some discrepancies in the temperature profiles between the different meshes, with the finer meshes predicting higher temperature distribution inside the cavity region. The differences in temperature distributions were expected because of the different mesh refinements necessary to calculate the heat exchange at the interfaces between fluid and solid regions (i.e., where conjugate heat transfer is present). Figure 6 also shows a local maximum in the air temperature in proximity of the RPV flange. The flange represents an obstruction for the thermal boundary layer developing along the RPV wall, and a local minimum in the axial velocity is present close to the RPV wall at the flange location. This explains why the air temperature shows a local maximum close to the flange. The air temperature progressively increases from the RCCS bottom wall toward the upper part of the cavity as the air becomes lighter and cools down the RPV wall. The maximum air temperature is reached in the upper part of the cavity.

Figure 7 shows the radial temperature distribution at the cavity region symmetry plane 275 mm from the bottom wall for test 2. In the upper part of the RCCS cavity region, the effect of mesh refinement on the temperature distribution is even more evident, with a difference of ~40 K among the different meshes analyzed and the finer meshes predicting higher temperature distributions across the cavity region.

Figure 8 shows the axial temperature distribution at the cavity back wall (rack plane location) for test 3. For this analysis the back wall temperature does not exceed 340 K, which is slightly larger than the maximum values reached for test 1 and test 2 (320 and 325 K, respectively). This temperature is still well below the design limits for the cavity concrete walls. It is possible to conclude that for the very high RPV temperature conditions reached in test 3, the water-cooled RCCS system is still capable of keeping the RCCS external walls temperature below design limits.

In Fig. 9 the velocity vector distribution in the RCCS cavity region at the rack plane location for test 3 is shown. The velocity vector plot shows the main recirculation region in the upper half of the RCCS cavity region between the RPV wall and the standpipes wall. In addition, the stagnant region below the RPV lower head and the secondary recirculation region above the RPV upper head can be identified.

Figure 10 shows the axial velocity distribution in the radial direction at the cavity region symmetry plane 215 mm from the bottom wall for test 3. The figure shows the effect of buoyancy forces on the velocity distribution close to the RPV wall. The finer meshes predict with greater accuracy the temperature gradient across the thermal boundary layer, which means a better estimate of the buoyancy forces can be determined. Since buoyancy forces are the driving phenomena in free convection flow regime, a better estimate of the velocity profile close to the RPV wall is obtained for the finer meshes.

Figures 11 and 12 show the axial temperature distribution at the cavity region rack plane 0.25 mm from the RPV wall and at the cavity back wall, respectively (test 3). The figures show the comparison between the different turbulence models analyzed. In particular, for test 3 the following turbulence models were tested: the realizable k-ε model with two-layer *all* y^+ wall treatment, the AKN k-ε model with low Reynolds number and *all* y^+

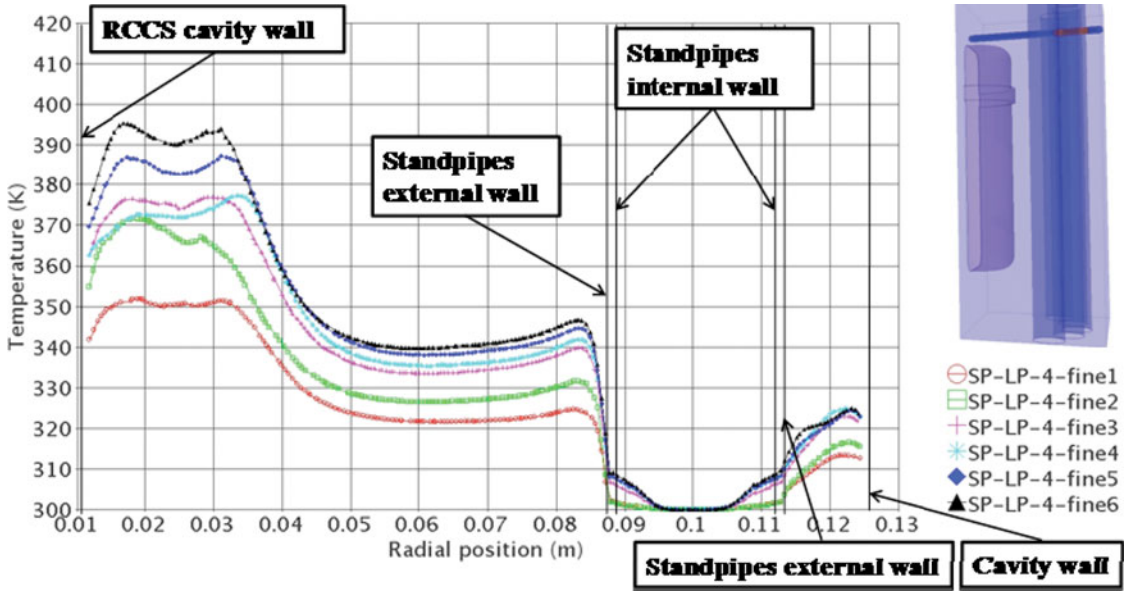

Fig. 7. Mesh sensitivity for the cavity region radial temperature distribution 275 mm from the bottom wall (symmetry plane)—test 2.

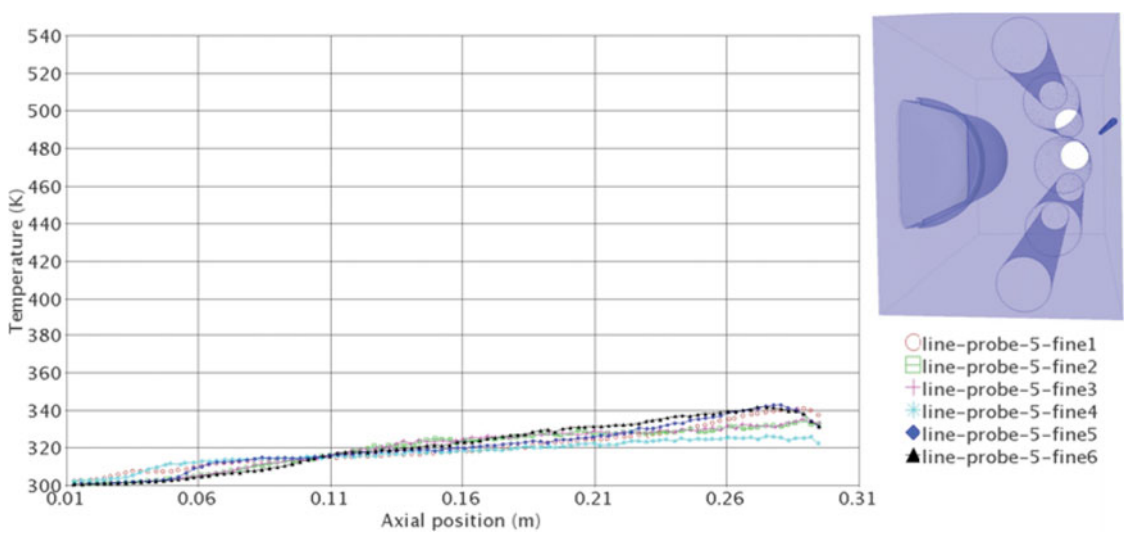

Fig. 8. Mesh sensitivity for the cavity region back wall axial temperature distribution (rack plane)—test 3.

wall treatment, the SST k-ω model with *all* y^+ wall treatment, the RST with two-layer *all* y^+ wall treatment, the Spalart-Allmaras one-equation model with *all* y^+ wall treatment, and the standard k-ε model with two-layer *all* y^+ wall treatment. For the temperature distribution a good agreement between the different turbulence models was achieved. The standard and realizable k-ε models gave very close temperature distribution prediction, and both models gave a qualitative and quantitative good agreement with the RST turbulence model. The AKN k-ε model, the SST k-ω model, and the Spalart-Allmaras one-equation model show some differences with respect to the RST in the central part of the RCCS region. This different behavior of the AKN, k-ω, and Spalart-Allmaras models is due to the different predictions in the extension of the main recirculation region inside the cavity medium. As the comparison among the different turbulence models for the axial velocity distribution in the cavity region shows (see Figs. 13 and 14), there are some differences at the bottom part of the cavity region where the air moving downward is redirected toward the RPV wall. At the cavity back wall (see Fig. 12) there is good

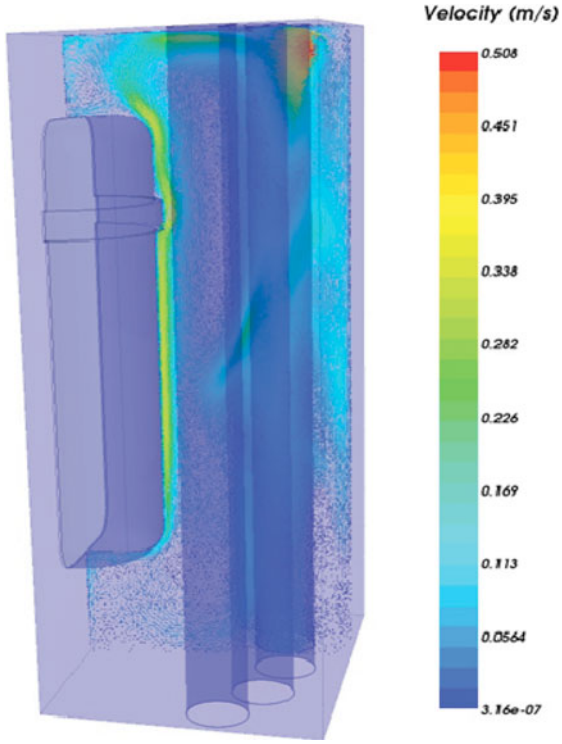

Fig. 9. Velocity vector in the RCCS cavity region (rack plane)—test 3.

agreement among the different turbulence models analyzed since the temperature gradients and buoyancy effects are much less relevant than close to the RPV wall.

Figures 13 and 14 show the radial distribution of the axial velocity at the cavity region symmetry plane, 135 mm and 275 mm from the bottom wall, respectively (test 3). The figures show that there are some discrepancies between the different turbulence models analyzed in predicting the extension of the main recirculation region in the lower part of the cavity (see Fig. 13) and in the upper part of the cavity (see Fig. 14). Because of the strong anisotropy of the Reynolds stress tensor and the 3-D characteristics of the turbulence in the cavity region, the RST model is expected to give a better prediction of the flow inside the cavity region.

Figures 13 and 14 also show that the axial velocity distributions determined with the realizable and standard k-ε model and two-layer *all* y^+ near-wall treatment are very close to that predicted with the RST turbulence model; meanwhile, the AKN k-ε, the SST k-ω, and the Spalart-Allmaras models underestimate/overestimate the extension of the main recirculation region, the effect of buoyancy close to the RPV wall, the temperature distribution in the thermal boundary layer, etc.

The CFD simulations allow determination of the fraction of energy transferred to the standpipes by radiation and convection heat transfer mechanisms, respectively. For the boundary conditions set in test 3, the CFD simulation predicted values of 59.4% and 40.6% due to radiation and convection heat transfer phenomena, respectively. The scaling analysis allowed a rough estimate of the heat transfer fraction because of radiation and convection mechanisms. For test 3 the respective values were 53.5% and 46.5%, with an error between the scaling analysis and the CFD simulation of the 10%. Radiation heat transfer is becoming the predominant heat transfer mechanism because of the increase in the

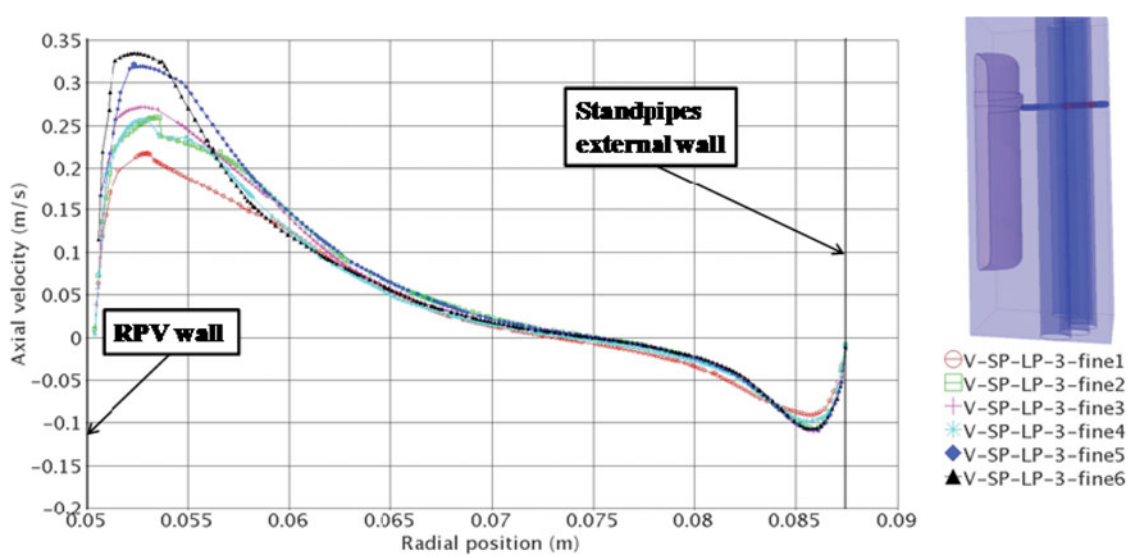

Fig. 10. Mesh sensitivity for the cavity region axial velocity 215 mm from the bottom wall (symmetry plane)—test 3.

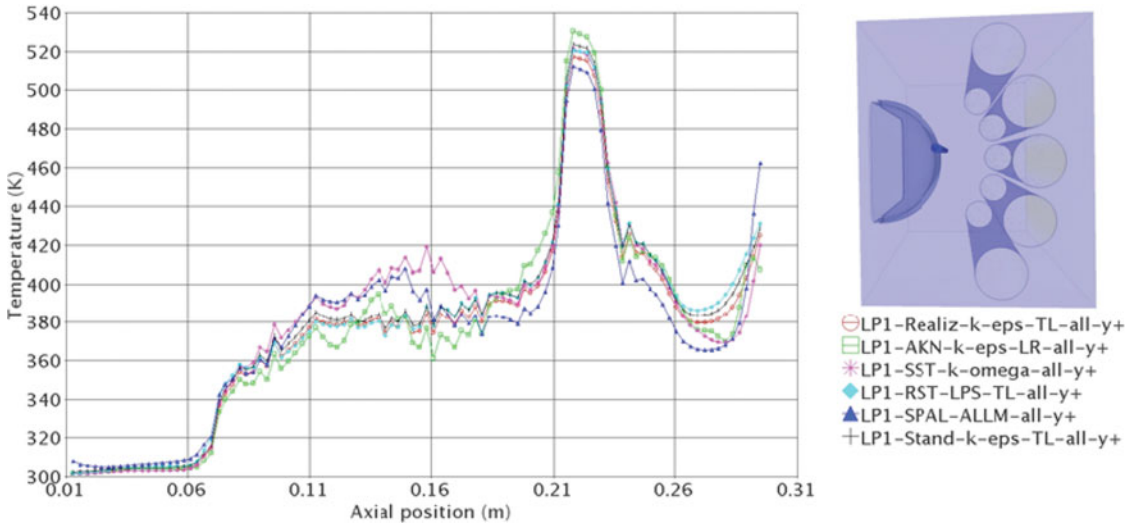

Fig. 11. Turbulence models comparison for the cavity region axial temperature distribution 0.25 mm from the RPV wall (rack plane)—test 3.

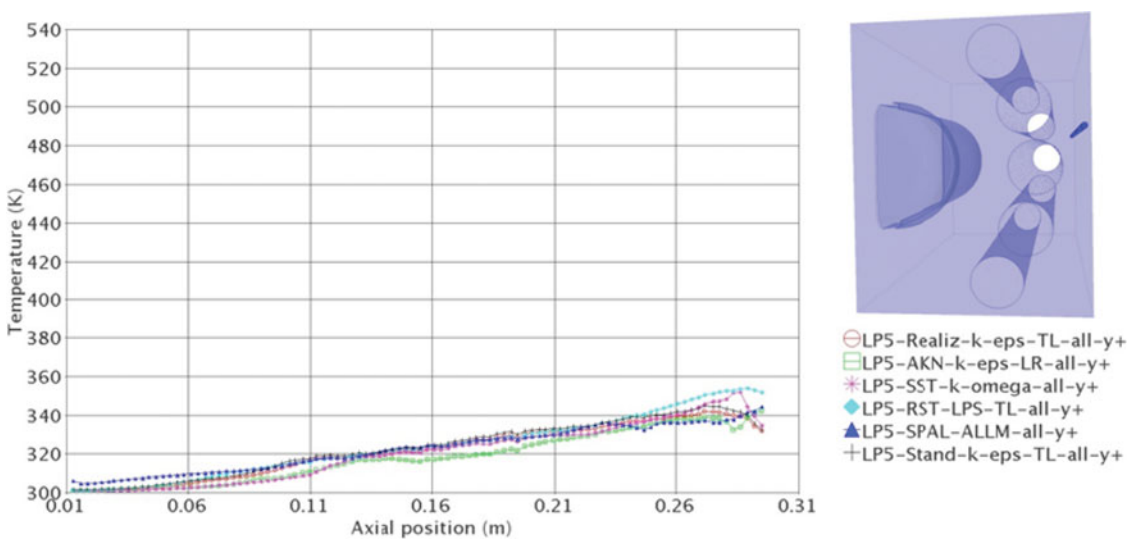

Fig. 12. Turbulence models comparison for the cavity region back wall axial temperature distribution (rack plane)—test 3.

temperature gradient across the cavity (i.e., RPV temperature).

For this analysis the ratio of Ri number is very close to 1 (see Table III), which means that the momentum equation in the standpipes is properly scaled from the prototype down to the model. Also, the ratio of Gr/Re^2 in the cavity region is very close to 1, which means the effect of buoyancy forces over inertia forces is not distorted, and the physics inside the cavity region is well represented.

Since the effect from radiation and convection heat transfer numerically determined is in good agreement with that calculated by the scaling analysis, it is possible to conclude that the scaling distortion introduced by the CFD model on radiation and convection heat transfer is of the same order, and therefore, the two heat transfer phenomena are properly scaled by the CFD model.

Figures 15 through 18 show the experimental results for the axial temperature distribution inside the RCCS cavity (rack plane location) at 0.25, 25.4, 38.1, and 50.8 mm from the reactor vessel wall, respectively. The figures also show the temperature distribution determined by the STRAR-CCM+ code for the different turbulence models analyzed (test 4). The figures show that the computational results are close to the experimental data, especially in the upper part of the RCCS cavity

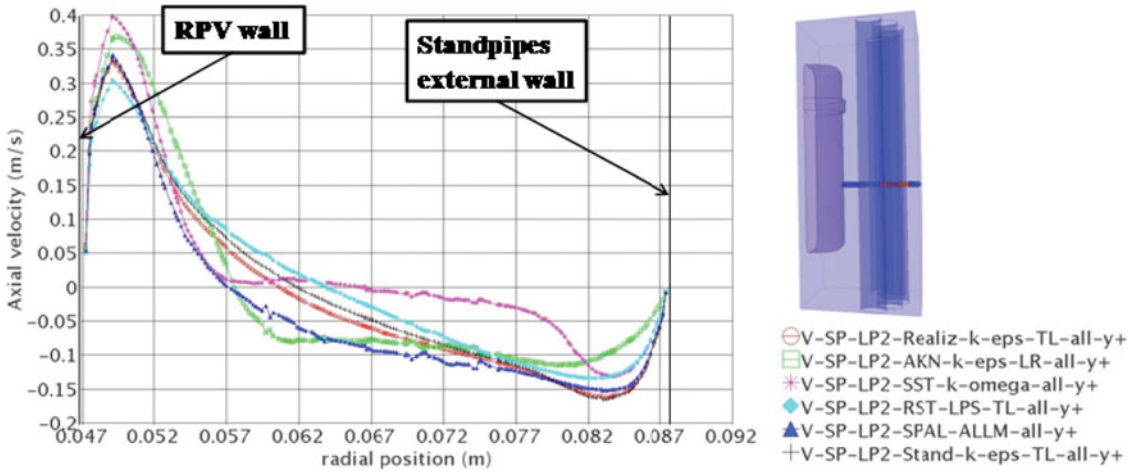

Fig. 13. Turbulence models comparison for the cavity region axial velocity distribution 135 mm from the bottom wall (symmetry plane)—test 3.

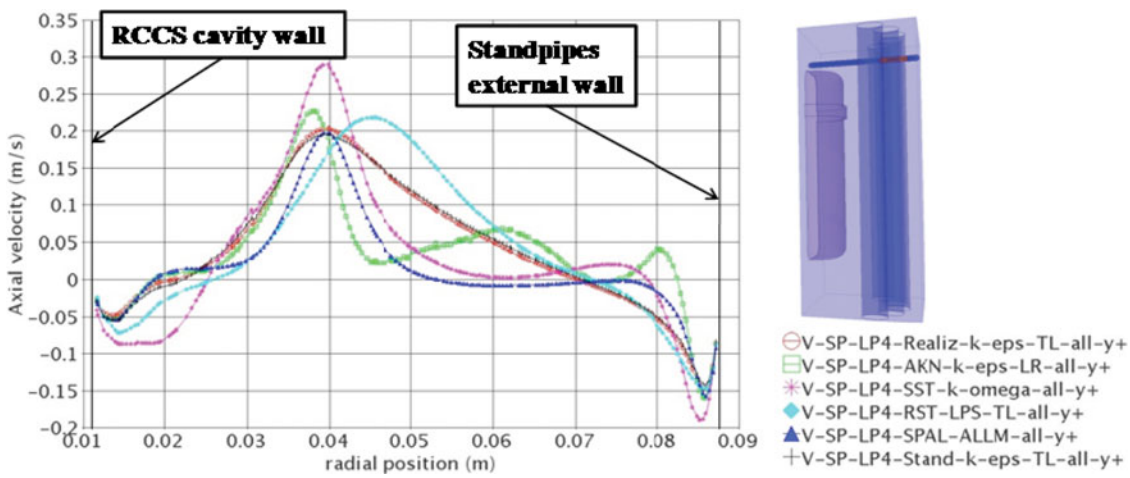

Fig. 14. Turbulence models comparison for cavity region axial velocity distribution 275 mm from the bottom wall (symmetry plane)—test 3.

region. Some differences between the experimental data and the numerical results were present in the lower part of the RCCS cavity region. These discrepancies between computational and experimental results were due to the bottom part of the RCCS cavity wall. In the experimental facility the bottom cavity wall was partially made of aluminum, while glass was assumed for the CFD model. The aluminum in the mock-up determined a higher temperature for the lower part of the RCCS cavity due to radiation heat exchange between the RPV wall and the external box (i.e., back radiation from the bottom wall in the cavity region). This behavior is not shown in the CFD simulations, since the bottom wall is at a lower temperature than the air in the RCCS cavity region. Because of this discrepancy between the experimental facility and the CFD model, the air temperature in the lower part of the mock-up cavity region is higher than the air temperature in the CFD model cavity region. Notwithstanding the differences between the CFD numerical simulations and the experimental data, it is possible to say that the numerical results show a good qualitative agreement with the experimental data.

Considering the sensitivity analysis over the different turbulence models analyzed, the figures show that all turbulence models can qualitatively predict the correct temperature distribution inside the RCCS cavity, with relatively small differences among the models analyzed. In general, it is possible to say that the k-ε models performed better than the k-ω models, if compared to both the experimental data and the RST results. Among the

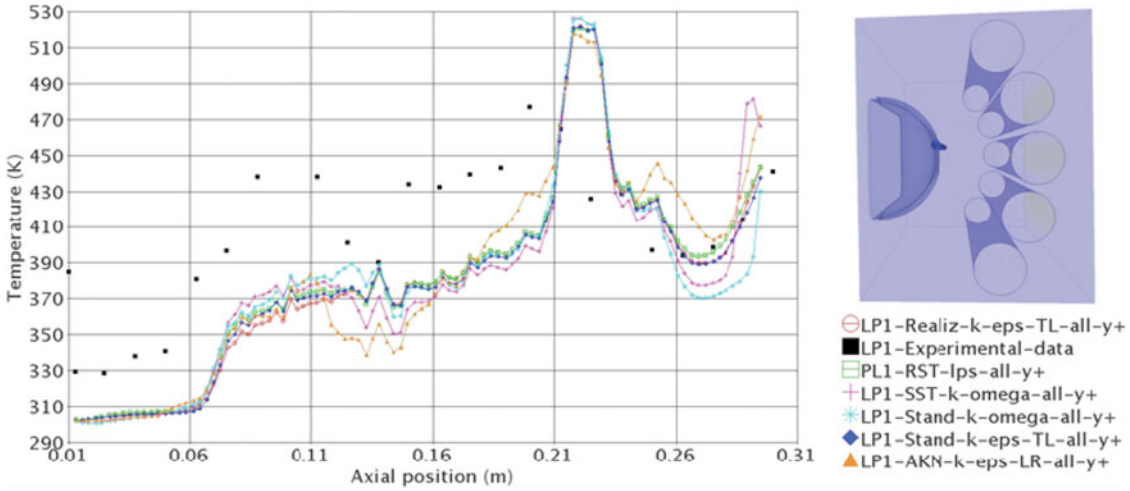

Fig. 15. Cavity region axial temperature distribution 0.25 mm from the RPV wall (rack plane)—test 4.

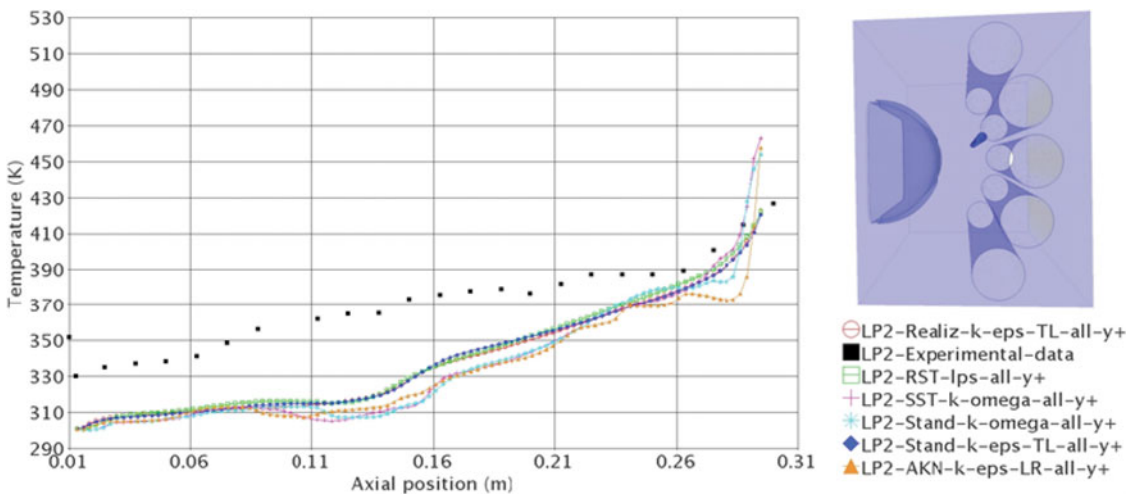

Fig. 16. Cavity region axial temperature distribution 25.4 mm from the RPV wall (rack plane)—test 4.

k-ε turbulence models analyzed, the ones using the two-layer approach performed better than the turbulence models using the low–Reynolds number approach. For the treatment of the wall region, the *all* y^+ methodology resulted in a better convergence if compared to the *low* y^+ approach.

The realizable k-ε turbulence model performed better than the standard and the AKN k-ε models.

In Fig. 15 it is possible to note the sharp air temperature increase in proximity of the RPV bottom head (i.e., ~0.06 m from the cavity bottom wall). The figure also shows the increase of air temperature along the RPV wall (i.e., buoyancy forces drive the air upward) and the sharp increase in the air temperature close to the RPV flange (i.e., ~0.21 m from the cavity bottom wall). The concave shape of the temperature distribution in the upper part of the cavity is due to the presence of the main recirculation region, which moves colder air toward the upper part of the cavity region.

The temperature trend shown in Figs. 16, 17, and 18 is similar to the one close to the RPV wall, with a smoother temperature gradient across the cavity height. Also, the temperature measurements close to the central standpipe (i.e., Figs. 17 and 18) show that the air temperature in the bottom part of the cavity region is almost constant. This addresses the fact that the bottom part of the cavity region is almost at stagnant conditions, with the recirculation region due to buoyancy effects developing in the upper part of the cavity.

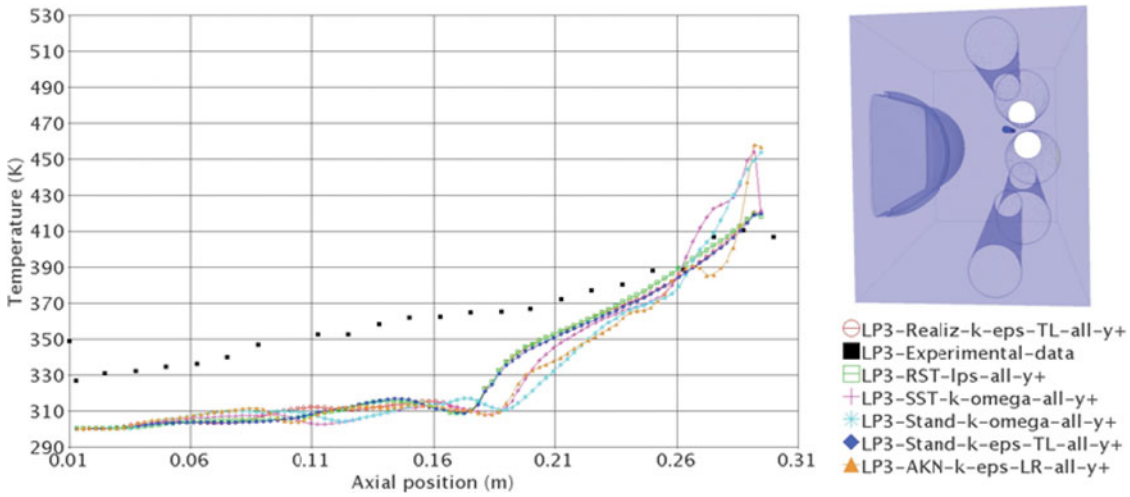

Fig. 17. Cavity region axial temperature distribution 38.1 mm from the RPV wall (rack plane)—test 4.

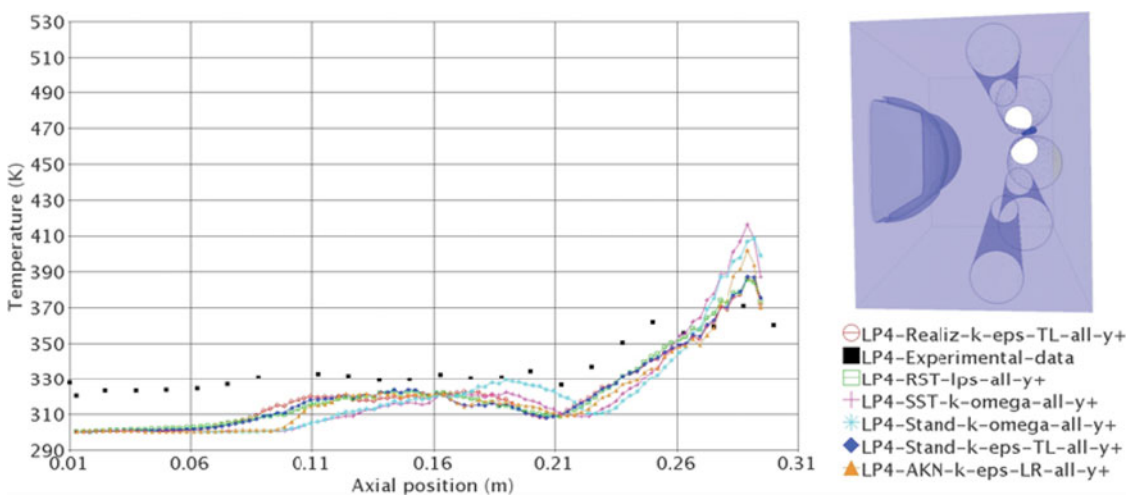

Fig. 18. Cavity region axial temperature distribution 50.8 mm from the RPV wall (rack plane)—test 4.

For the boundary conditions set in test 4, the CFD simulation determined values of 54% and 46% from radiation and convection heat transfer, respectively. The respective values determined by the scaling analysis were 60.8% and 39.2%, with an error equal to 11.2%.

VI.B. Analysis of the RCCS Air-Cooled Configuration (Tests 5 Through 9)

Tests 5 through 9 consider the RCCS in the air-cooled configuration, where air is flowing inside the standpipes. A constant mass flow rate was imposed at the standpipe inlets, while different temperature profiles were set at the RPV wall boundary in such a way to simulate a range of working conditions for the RPV wall and for the RCCS cavity region. With a uniform heat source imposed inside the RPV region as boundary condition (see tests 1, 2, and 3), an almost uniform temperature distribution is obtained at the RPV wall due to the very high thermal conductivity of the material chosen for the RPV (i.e., Cu). On the other hand, the power generated inside the RPV does not have a uniform distribution during either normal operation or accident conditions. With the reactor in shutdown conditions (e.g, following a scram due to an accident scenario), the largest part of energy generated inside the RPV is due to the decay heat of the reactor core. Other sources of heat are the thermal energy stored inside the reactor vessel internals and the γ heating on the RPV walls and other metallic components close to the core region. It is very difficult to make an exact prediction of the energy distribution inside the RPV and the heat

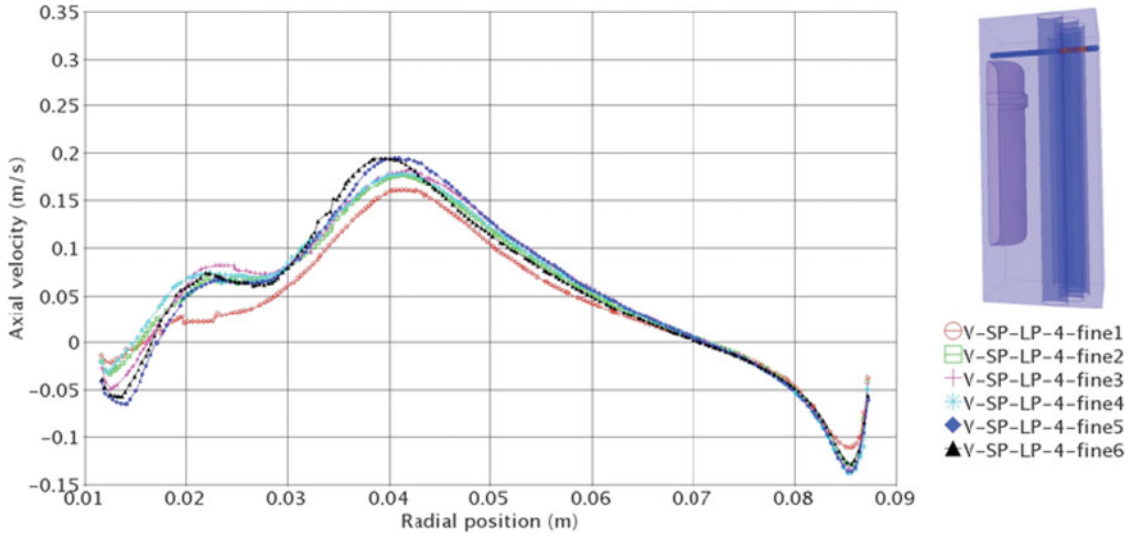

Fig. 19. Mesh sensitivity for the cavity region axial velocity distribution 275 mm from the bottom wall (symmetry plane)—test 8.

flux at the RPV wall. From experimental data,[11] it was possible to have a rough estimate of the heat fluxes at the RPV wall during the different phases of PCC and DCC scenarios, which give temperature distributions qualitatively similar to those used for tests 4 through 8. The objective of these analyses was to test the performance of the RCCS air-cooled configuration, imposing temperature profiles at the RPV wall that take into account the nonuniform distribution of heat generated inside the vessel and address the behavior of the RCCS system for the boundary conditions set.

Figure 19 shows the axial velocity distribution in the radial direction at the cavity region symmetry plane 275 mm from the bottom wall (i.e., above the RPV upper head) for test 8. The mesh sensitivity shows that also for the air-cooled configuration, there are some differences in the extension of the main and secondary recirculation regions in the cavity above the RPV upper head (i.e., the location of the separation and reattachment points on the RPV upper head), which address mesh convergence issues.

The axial temperature distribution at the cavity back wall rack plane location is shown in Fig. 20. In general for the air-cooled RCCS configuration, coarser meshes predict higher air temperature distribution across the cavity region, if compared to finer meshes for the cases

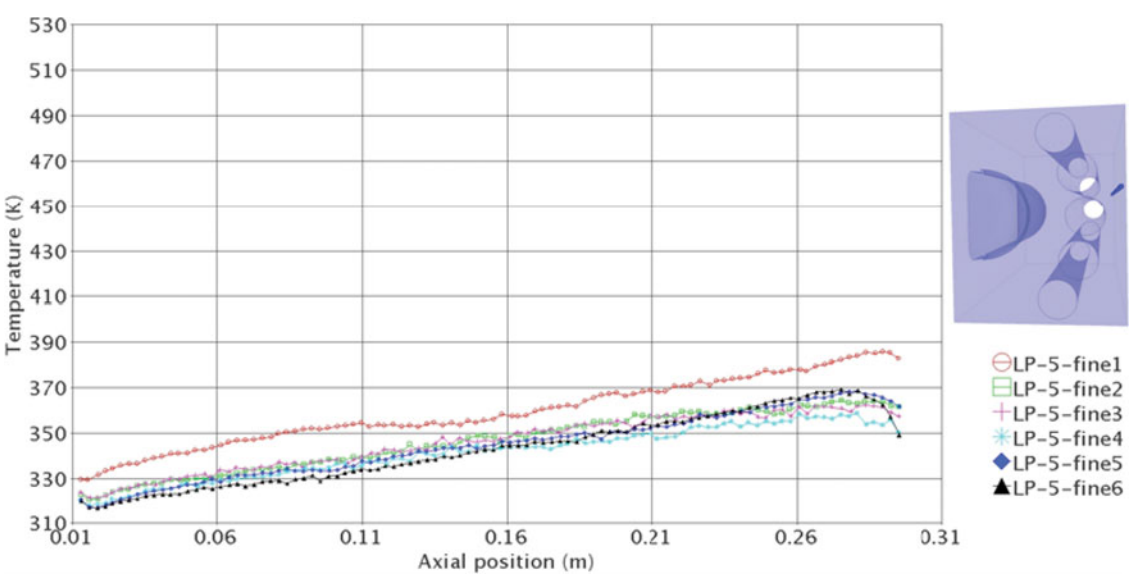

Fig. 20. Mesh sensitivity of the cavity region back wall axial temperature distribution (rack plane)—test 8.

analyzed. Also for test 8, the mesh sensitivity analysis shows that the coarsest mesh predicts a higher temperature distribution on the cavity back wall with respect to the finer meshes. The maximum temperature is reached close to the cavity top wall. The figure shows that the maximum temperature ranges from 370 to 390 K, which is the temperature for which the concrete material starts to show an increase in the rate of properties deterioration.

Figure 21 compares the temperature distribution at the cavity back wall (rack plane location) for tests 1 through 9. For tests 1, 2, and 3, a uniform volumetric heat source inside the RPV region was imposed, for a total power generated equal to 27.0, 50.0, and 170.0 W, respectively. The cooling fluid in the standpipes was water (see Sec. VI.A). Test 4 resembled the boundary conditions imposed in the experimental facility. The total energy generated inside the RPV region equals 196 W. For tests 5 through 9 the same standpipes air mass flow rate was imposed. On the other hand, the different temperature profiles imposed at the RPV wall for tests 5 through 9 determined a different amount of energy generated inside the RPV region: 23.4, 43.16, 65.5, 104.2, and 131.0 W, respectively. Figure 21 shows that the maximum temperature is reached close to the cavity top wall for all analyses. The air-cooled configurations give a higher air temperature distribution inside the RCCS cavity region and at the cavity walls with respect to the water-cooled configurations. Comparing test 4 (water-cooled configuration with 196 W RPV total power generated) with test 9 (air-cooled configuration with 130 W RPV total power generated), it is evident that even with 30% less power generated, the air-cooled configuration gives a maximum temperature on the cavity walls of ~395 K, almost 45 K higher than the maximum temperature reached for test 4 (~350 K). These results demonstrate the better performance of the water-cooled RCCS configuration with respect to the air-cooled one.

Considering the results obtained for the RCCS air-cooled configuration, for tests 5, 6, and 7, the maximum concrete wall temperature is below the design limits, while for test 8 it is very close to the design limits. With the boundary conditions set for test 9, the maximum temperature at the cavity walls is above the design limits.

The CFD simulations with the boundary conditions set for test 9 predicted 87.8% and 12.2% heat transfer due to radiation and convection phenomena, respectively. The scaling analysis predicted 83.7% and 16.3% for radiation and convection heat transfer, respectively, with an error rate <4.7%.

For this analysis the ratio of Gr/Re^2 is 1.044, which means no distortion is introduced in scaling buoyancy over inertia forces from the real plant down to the CFD model. In addition, the ratios of convection and radiation numbers are close to unity, which means that the physics inside the RCCS cavity is well scaled by the CFD model.

VII. CONCLUSION

The objective of the present work was to apply CFD tools to the analysis of the RCCS, which is one of the safety systems designed for VHTRs.

The scaling analysis performed pointed out that the mock-up/CFD model well addresses the physics inside the RCCS cavity region for a wide range of operating conditions and both water-cooled and air-cooled RCCS configurations. Buoyancy over inertia forces

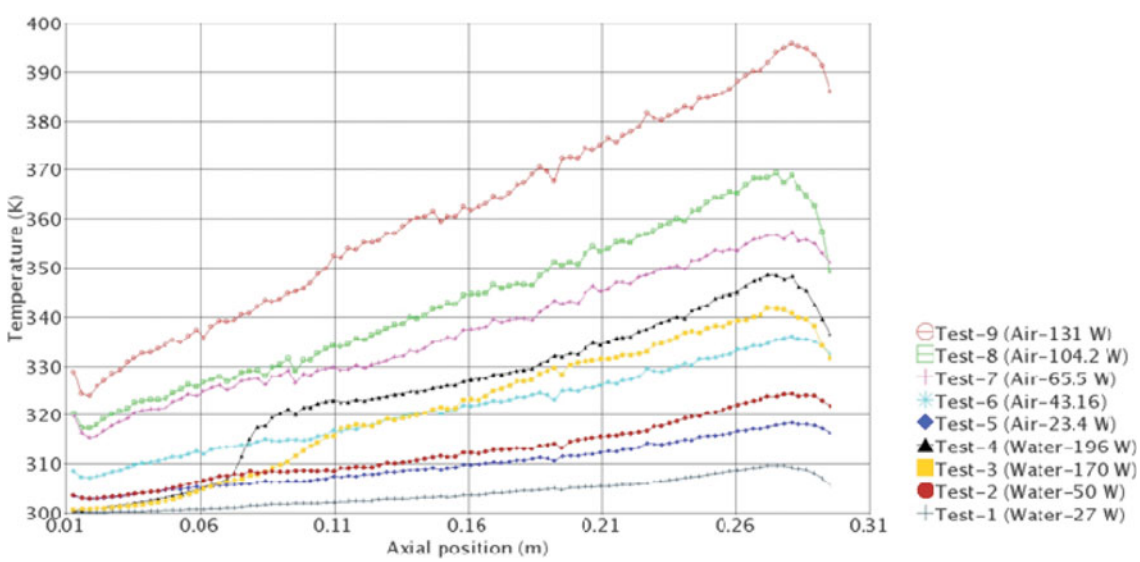

Fig. 21. Comparison of the cavity region back wall axial temperature distribution (rack plane)—tests 1 through 9.

are properly reproduced inside the models. The correct repartition of energy transfer by radiation and convection is predicted in the experimental facility and CFD model for both water- and air-cooled configurations. The numerical sensitivity performed with the CFD model showed that the natural circulation conditions can be simulated for the model setting a very low standpipes mass flow rate.

Buoyancy effects are distorted in the model developed because of the physics of the problem, which is the reduced heated length considered.

For the numerical simulations, the sensitivity analysis over the different turbulence models showed that the realizable and standard k-ε models with two-layer *all* y^+ near-wall treatment perform better than the SST and standard k-ω models, the AKN k-ε model, and the Spalart-Allmaras one-equation model, showing closer agreement with the experimental data and the RST turbulence model.

The RST model was expected to perform much better than the k-ε models in determining the conjugate heat transfer close to the RPV wall, where very strong temperature gradients and 3-D turbulence effects are present. The results showed that no sensible differences were present between the simulations performed with the RST turbulence model and those realized with the realizable and standard k-ε models, even if the computational effort was strongly increased. The reason for such a behavior is partially due to a coarse mesh discretization outside the prism layer region close to the RPV wall, and also to the fact that the flow regime inside the RCCS cavity region is not completely turbulent. Some stratification regions in the lower part of the cavity can be identified where return to laminar conditions might be present. These conditions are extremely arduous to simulate even for the most advanced commercial CFD codes, if the closure problem of the momentum and energy equations is resolved by using first- or second-moment closure equations. Perhaps the best way to approach this problem would be to use large-eddy simulation methodologies, where a negligible part of the turbulence dissipation is modeled and the main structures of the flow are completely resolved.

The sensitivity over mesh convergence showed that the results are extremely dependent on the mesh refinement at the fluid-solid interface. In particular, the region close to the RPV wall requires very fine meshes because of the large temperature gradients at the wall. These temperature gradients sensibly influence the buoyancy effects close to the vessel wall and, therefore, the flow regime inside the RCCS cavity. Also, the change of fluid properties plays a dominant role in determining the buoyancy effects inside the RCCS cavity region.

A key strength of CFD codes is their ability to simulate radiation heat exchange phenomena in very complex geometries, where the determination of view factors represents the main problem for analytical solution of the problem.

REFERENCES

1. S. KIM, N. I. TAK, H. S. LIM, and S. J. HA, "Sensitivity Study on Depressurized LOFC Accidents with Failure of RCCS in a Modular Gas-Cooled Reactor," *J. Ann. Nucl. Eng.*, **37**, 664 (2010).

2. R. R. SCHULTZ, "Next Generation Nuclear Plant Methods Technical Program Plan," INL/EXT-06-11804, Idaho National Laboratory (Jan. 2007).

3. Y. S. SIM, R. Y. PARK, and S. KIM, "Development of a New Decay Heat Removal System for a High Temperature Gas-Cooled Reactor," *J. Ann. Nucl. Eng.*, **34**, 803 (2007).

4. A. MATEV, "Simulation of the Operation in Passive Mode of a Reactor Cavity Cooling System of High-Temperature Gas-Cooled Reactor," *Proc. 16th Int. Conf. Nuclear Engineering*, Orlando Florida, May 11–15, 2008, American Society of Mechanical Engineers (2008).

5. J. P. SIMONEAU, J. CHAMPIGNY, B. MAYS, and L. LOMMERS, "Three-Dimensional Simulation of the Coupled Convective, Conductive, and Radiative Heat Transfer During Decay Heat Removal in an HTR," *J. Nucl. Eng. Des.*, **237**, 1923 (2007).

6. M. P. VAN STADEN, "Analysis of Effectiveness of Cavity Cooling System," 2nd Int. Topl. Mtg. High Temperature Reactor Technology, Beijing, China, September 22–24, 2004.

7. C. OH, E. KIM, R. SCHULTS, M. PATTERSON, D. PETTI, and H. KANG, "Comprehensive Thermal Hydraulics Research of the Very High Temperature Gas Cooled Reactor," *J. Nucl. Eng. Des.*, **240**, 3361 (2010).

8. K. HOSSAIN, M. BUCK, N. BEN SAID, W. BERNNAT, and G. LOHNERT, "Development of a Fast 3D Thermal-Hydraulic Tool for Design and Safety Studies for HTRS," *J. Nucl. Eng. Des.*, **238**, 2976 (2008).

9. M. H. KIM, H. S. LIM, and W. J. LEE, "A Thermal-Fluid Assessment of a Cooled-Vessel Concept for VHTR," *J. Nucl. Eng. Des.*, **238**, 3360 (2008).

10. "STAR-CCM+ Version 3.06.006 User Guide," Computational Dynamics Limited (2008).

11. "Heat Transport and Afterheat Removal for Gas Cooled Reactors Under Accident Conditions," IAEA-TECDOC-1163, International Atomic Energy Agency (2000); http://www.iaea.org/inisnkm/nkm/aws/htgr/abstracts/abst_crp3.html (current as of May 25, 2010).

12. S. J. BALL, "MHTGR Accident Analysis," American Nuclear Society MHTGR Technology Course (June 2003).

13. K. KRÜGER, A. BERGERFURTH, S. BURGER, P. POHL, M. WIMMERS, and J. C. CLEVELAND, "Preparation, Conduct, and Experimental Results of the AVR Loss-of-Coolant Accident Simulation Test," *Nucl. Sci. Eng.*, **107**, 99 (1991).

14. L. CAPONE, C. E. PEREZ, and Y. A. HASSAN, "Experimental Investigation of the Reactor Cavity Cooling System

(RCCS) for a Very High Temperature Reactor (VHTR)," *Proc. 18th Int. Conf. Nuclear Engineering*, Xi'an, China, May 17–21, 2010, American Society of Mechanical Engineers (2010).

15. A. FRISANI, L. CAPONE, V. M. UGAZ, and Y. A. HASSAN, "Three Dimensional Simulation of RCCS Heat Exchange Using STAR-CCM+ CFD Code," *Trans. Am. Nucl. Soc.*, **100**, 685 (2009).

16. A. FRISANI, V. UGAZ, and Y. A. HASSAN, "On the Effect of Turbulence Modeling and Near-Wall Treatment in Simulating Heat Exchange in the Reactor Cavity Cooling System Using STAR-CCM+ CFD Code," *Trans. Am. Nucl. Soc.*, **101**, 881 (2009).

17. R. B. VILIM and E. E. FELDMAN, "Scalability of the Natural Convection Shutdown Heat Removal Test Facility (NSTF) Data to VHTR/NGNP RCCS Designs," ANL-GenIV-049, Argonne National Laboratory (June 2005).

18. F. S. LIEN, W. L. CHEN, and M. A. LESCHZINER, "Low-Reynolds Number Eddy-Viscosity Modeling Based on Non-Linear Stress-Strain/Vorticity Relations, *Proc. 3rd Symp. Engineering Turbulence Modeling and Measurement*, Crete, Greece, May 27–29, 1996.

19. W. P. JONES and B. E. LAUNDER, "The Prediction of Laminarization with a Two-Equation Model of Turbulence," *Int. J. Heat Mass Transfer*, **15**, 301 (1972).

20. B. E. LAUNDER and B. I. SHARMA, "Application of Energy Dissipation Model of Turbulence to the Calculation of Flow Near a Spinning Disc," *Lett. Heat Mass Transfer*, **1**, *2*, 131 (1974).

21. T. H. SHIH, W. W. LIOU, A. SHABBIR, Z. YANG, and J. ZHU, "A New k-ε Eddy Viscosity Model for High Reynolds Number Turbulent Flows—Model Development and Validation," NASA TM 106721, National Aeronautics and Space Administration (1997); http://ntrs.nasa.gov/ (current as of May 25, 2010).

22. K. ABE, T. KONDOH, and Y. NAGANO, "A New Turbulence Model for Predicting Fluid Flow and Heat Transfer in Separating and Reattaching Flows—1. Flow Field Calculation," *Int. J. Heat Mass Transfer*, **37**, 1 (1991).

23. D. C. WILCOX, *Turbulence Modeling for CFD*, 2nd ed., DCW Industries, Inc. (1998).

24. F. R. MENTER, "Two-Equation Eddy-Viscosity Turbulence Modeling for Engineering Applications," *IAAA J.*, **3**, *8*, 1598 (1994).

25. M. M. GIBSON and B. E. LAUNDER, "Ground Effects on Pressure Fluctuations in Atmospheric Boundary Layer," *J. Fluid Mech.*, **86**, *3*, 491 (1978).

26. S. SARKAR and L. BALAKRISHNAN, "Application of a Reynolds-Stress Turbulence Model to the Compressible Shear Layer," ICASE Report 90-18, NASA CR 182002, Institute for Computer Applications in Science and Engineering (1990).

27. C. G. SPEZIALE, S. SARKAR, and T. B. GATSKI, "Modeling the Pressure-Strain Correlation of Turbulence: An Invariant Dynamical Systems Approach," *J. Fluid Mech.*, **227**, 245 (1991).

28. P. R. SPALART and S. R. ALLMARAS, "A One-Equation Turbulence Model for Aerodynamic Flows," *Proc. 30th Aerospace Sciences Mtg.*, Reno, Nevada, January 6–9, 1992, AIAA-92-03439, American Institute of Aeronautics and Astronautics (1992).